Miner Petrol (2016) 110:927–942
DOI 10.1007/s00710-016-0440-8

ORIGINAL PAPER

Using the chemical analysis of magnetite to constrain various stages in the formation and genesis of the Kiruna-type chadormalu magnetite-apatite deposit, Bafq district, Central Iran

Hassan Heidarian[1] · **David Lentz**[2] · **Saeed Alirezaei**[1] · **Sima Peighambari**[3] · **Douglas Hall**[2]

Received: 30 September 2015 / Accepted: 15 March 2016 / Published online: 22 March 2016

Abstract Textural and compositional data are presented for different types of magnetite in the Chadormalu iron deposit to discern the genesis of various styles of mineralization. Samples were chosen according to their paragenetic relations to apatite and their host setting: magnetite-apatite veins in the altered host rocks, disseminated magnetite-apatite assemblages in the marginal parts of the main ore body, and massive magnetite associated with irregular apatite veinlets from internal part of the main ore body. Scanning electron microscopy - back scatter electron (SEM-BSE) images reveal that there are three main generations of magnetite in each of the different magnetite-apatite assemblages. Primary magnetite (Mag1) features abundant porosity and a dark appearance. A second generation of magnetite (Mag2) replacing Mag1 shows a lighter appearance with both sharp and gradational contacts with the primary magnetite crystals. The two magnetite types are related to dissolution-precipitation processes due to changing physico-chemical parameters of the ore fluids. A third type of magnetite (Mag3) with a recrystallized appearance and foam-like triple junctions was mostly observed in magnetite-apatite veins in the main ore body and in veins hosted by altered rocks. Electron probe microanalyses (EPMA) were utilized to discriminate the various magnetite generations in the different magnetite-apatite assemblages. Applying published elemental discrimination diagrams shows that most primary magnetites fall into the hydrothermal- and Kiruna-type fields. Primary magnetite contains lower FeO (88.77–93.65 wt.%; average 91.5 wt.%), and higher SiO_2 (0.21–2.26 wt.%; ave. 0.32 wt.%), Al_2O_3 (0.001–0.45 wt.%; ave. 0.053 wt.%), and CaO (0.002–0.48 wt.%; ave. 0.078 wt.%) contents, which might be related to magmatically derived fluids. Secondary magnetites have higher FeO (89.23–93.49 wt.%; ave. 92.11 wt.%), lower SiO_2 (0.037–0.189 wt.%; ave. 0.072 wt.%), Al_2O_3 (0.004–0.072 wt.%; ave. 0.019 wt.%), and CaO (<0.034 wt.%; ave. 0.013 wt.%) possibly showing a lower contribution of magmatic fluids in the formation of Mag2. The magnetite Mag3 contains the highest FeO (91.25–93.8 wt.%; average 92.69 wt.%), low to moderate SiO_2 (0.008–1.44 wt.%; ave. 0.13 wt.%), Al_2O_3 (<0.732 wt.%; ave. 0.059 wt.%), and CaO (<0.503 wt.%; ave. 0.072 wt.%), and appears to have formed by recrystallization of the previous two generations. The different major, minor, and trace element compositions of various magnetite generations might be due to an ore-forming fluid that was initially magmatic-hydrothermal and evolved to moderately brine-dominated meteoric fluids. The involvement of a basinal brine is supported by the occurrence of a late phase ^{34}S-enriched pyrite in the Chadormalu deposit.

Editorial handling: A. Beran

✉ Hassan Heidarian
ha.heidarian@gmail.com

[1] Faculty of Earth Sciences, Shahid Beheshti University, Evin, P.O. Box 1983963113, Tehran, Iran

[2] Department of Earth Sciences, University of New Brunswick, 2 Bailey Drive, Fredericton, NB E3B 5A3, Canada

[3] Department of Geology, Payame Noor University, P.O. Box 19395-3697, Tehran, Iran

Introduction

Magnetite is one of the most common minerals in various igneous, sedimentary, and metamorphic rocks. Also, magnetite occurs as an important iron ore phase in a variety of ore deposits, including BIF (banded iron formation), magmatic Fe/Ti oxides, and iron skarn deposits (Dupuis and

Beaudoin 2011; Huberty et al. 2012; Nadoll et al. 2012), as well as in many other types of hydrothermal deposits, such as IOCG (iron oxide–copper–gold), Kiruna-type apatite-magnetite, and porphyry systems (Williams et al. 2005; Liang et al. 2009).

There are two main different processes which are considered as the origin of Kiruna-type iron oxide-apatite (IOA) deposits. According to the first assumption, direct crystallization from a silicate magma can be responsible for the formation of massive magnetite bodies (Sillitoe and Burrows 2002), while the other hypothesis suggests that deposition from a hydrothermal fluid can produce large bodies of Fe-oxide-apatite ores (Barton 2014). However, Knipping et al. (2015) suggest a new model in which magnetite concentrations form from a silicate magma due to magma wetting followed by formation of suspended magmatic magnetite-bubble pairs that are then buoyantly segregated. Massive ore could be deposited from this magnetite suspension in transcurrent faults. The authors envisage this model as occurring in an arc magmatic system in which Cl-rich hydrous fluids form due to recycling of seawater during subduction.

The composition of minor and major elements of spinels can record the major processes controlling the formation of ore deposits (Barnes and Roeder 2001; Dupuis and Beaudoin 2011). Magnetite as a member of spinel mineral group hosts a wide variety of trace elements including Al, Ti, V, Si, Ca, Mn, and Mg (e.g. Dupuis and Beaudoin 2011; Nadoll et al. 2012). It is known that different physico-chemical parameters of magnetite-forming systems, including temperature, fO_2, fS_2, silica activity, and melt/fluid composition largely control the concentration and types of the trace elements in magnetite (Mücke 2003; Nadoll et al. 2012, and references therein; Hu et al. 2014, 2015). The trace elements can be useful in identifying different magnetite types and therefore might serve as genetic indicators of the ore deposits (Müller et al. 2003; Dupuis and Beaudoin 2011; Nadoll et al. 2012; Dare et al. 2014).

Magnetite can be replaced by hematite and/or new generations of magnetite by redox reactions in the course of ore formation (Mücke and Cabral 2005), or due to subsequent hydrothermal alteration. The hydrothermal replacement can change geochemically the primary magnetites from those enriched in certain constituents, including SiO_2, Al_2O_3, and MgO, towards secondary ones with lower SiO_2, Al_2O_3, and MgO (Hu et al. 2015). Accordingly, the geochemistry of texturally different magnetite generations may serve as a tool to distinguish the processes involved in the development of the mineral and related ore deposits (Hu et al. 2014, 2015). In this paper, textural and compositional data for magnetite from different magnetite-apatite types in the Chadormalu iron deposit are used in order to provide information about the genesis and evolution of the deposit.

Geological setting

The Bafq mining district lies in the Posht-e-Badam block (Stöcklin 1971; Haghipour 1977) or Kashmar-Kerman belt (Ramezani and Tucker 2003) in Central Iran (Fig. 1a, b). The belt is characterized by a Neoproterozoic basement sequence of Gondwanan affinity, consisting of various schists, gneisses, and granitic gneisses covered by Neoproterozoic to Triassic rocks (Stöcklin 1971; Borumandi 1973; Haghipour 1977; Förster and Jafarzadeh 1994). The Neoproterozoic and Cambrian rocks are extensively exposed in the arcuate Kashmar-Kerman belt situated between the Chapedony and Kuh-Banan faults (Jami et al. 2007; Fig. 1b, c). The basement consists of medium- to high-grade metamorphic rocks of the Boneh Shurow and Posht-e-Badam complexes intruded by intermediate intrusions (Jami et al. 2007). The Neoproterozoic-Early Cambrian rocks consist of phyllites, slates, quartzites, and mafic volcanic rocks of the Tashk Formation (Jami et al. 2007), covered by a terrestrial to shallow marine sequence containing Ediacaran fauna (Hahn and Pflug 1980) and an Early Cambrian (530–528 Ma) bimodal volcanic unit (Ramezani and Tucker 2003). Rhyolite and dacite flows and tuffs associated with subordinate andesite, spilitic basalt, and rare nephelinitic to basanitic lava flows are the main intercalated volcanic rocks in the district.

Samani (1993) divided the Cambrian Volcanic-Sedimentary Unit (CVSU) into three rock units, known as Saghand Formation and Rizu and Desu series. The type section for the Saghand Formation contains a basal conglomerate overlain by a lower volcanic unit consisting of 200 to 300 m of basaltic and rhyolitic lavas, followed by 150 to 200 m of shales and sandstones (Samani 1993). The upper volcanic unit contains over 400 m of lava flows, pyroclastic and epiclastic rocks, locally intercalated with limestones. The overlying Rizu and Desu series contain shales, carbonates, and evaporites and minor intercalated felsic and mafic volcanic rocks. Felsic centers are marked by rhyolites and intrusions of Narigan-type granites (Fig. 1c) (Jami et al. 2007). The sequence was intruded by small mafic to intermediate intrusive bodies and late doleritic dikes. All lithologies are locally subjected to syn-emplacement spilitization-keratophyric alteration (Jami et al. 2007).

The metasomatized CVSU and shallow intermediate to felsic intrusions are the main host rocks of the iron ore deposits in the Bafq district. The iron oxide ores are locally associated with REE-rich phosphate ± silicate ± carbonate assemblages, referred to as apatitite (Stosch et al. 2011). The timing of ore formation at Choghart has been constrained to be 515 ± 21 Ma and 529 ± 21 Ma (monazite Th-U- total Pb method; Torab and Lehmann 2007). Using isotopic U-Pb age dating, Stosch et al. (2011) reported 527 to 539 Ma for apatite samples from five iron deposits in the Bafq district. These ages fall in the age range of felsic plutonic and volcanic rocks in the

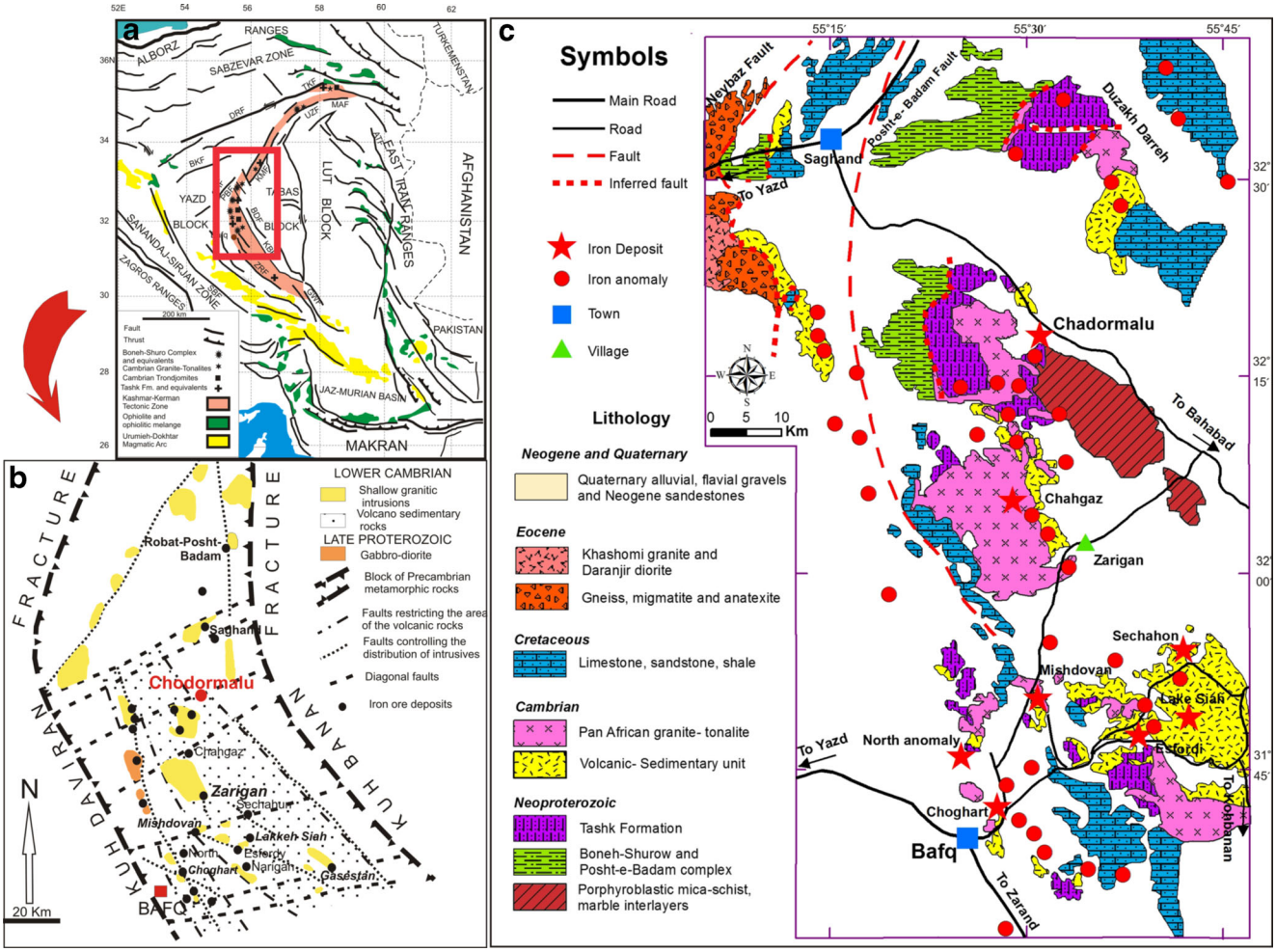

Fig. 1 **a, b** Distribution of iron oxide–apatite deposits in Kashmar-Kerman volcanic-plutonic belt (modified after Ramezani and Tucker 2003); **c** Modified geological map of Poshte-Badam area (modified from Haghipour 1977; NISCO 1980; Ramezani and Tucker 2003)

district (525–545 Ma, zircon U-Pb; Ramezani and Tucker 2003). However, using U–Pb LA-ICPMS, Bonyadi et al. (2011) reported a U–Pb LA-ICPMS age of 510 ± 8 Ma for the semi-massive ilmenite-rich magnetite and associated coarse REE-rich fluorapatite from Sechahun complex in the Bafq district. The authors reported an older age (525 ± 7 Ma) for sodic alteration from the same deposit.

The field relationships in Chadormalu are representative of a wide variety of alteration types occurring in different host rocks; this is schematically shown in Fig. 2. Sodic alteration, characterized by replacive albitization, is prevalent and widespread around the Chadormalu deposit. Ca-Fe alteration, dominated by actinolite occurs intensively in the marginal parts of the ore body and in the surrounding rocks. Silicification and carbonatization constitute two other types of alteration formed both during and after the sodic and calcic –ferroan alterations (Daliran et al. 2010; Sabet-Mobarhan-Talab et al. 2014; Heidarian et al. in review).

Magnetite, the major iron mineral in Chadormalu, is locally accompanied by hematite, ankerite, and siderite. Minor sulfide minerals dominated by pyrite locally formed during the late stages of magnetite mineralization. Other accessory minerals in the iron ore include apatite, calcite, and chlorite (Förster and Jafarzadeh 1984; Daliran et al. 2010; Heidarian 2013; Heidarian et al. in review).

Magnetite mineralization in Chadormalu occurs as two large massive bodies, including one in north (which is discussed hereafter as the main ore body and contains more than 80 % of the total ore reserve and, in turn, contains three distinctive bodies) (Fig. 2a) and one smaller body in south that displays faulted and brecciated contacts with metasomatized greenish host rocks. Magnetite also occurs as veins that sharply cut through the altered host rocks and contain fragments of host rocks locally displaying a brecciated appearance (Fig. 2b). The locations of the three main magnetite types discussed here are indicated in Fig. 2b; they include magnetite-apatite veins in the altered host rocks (classified as MAV-host rock), disseminated magnetite-apatite assemblages in the marginal parts of the main ore body (classified as MAA-marginal ore), and massive magnetite associated

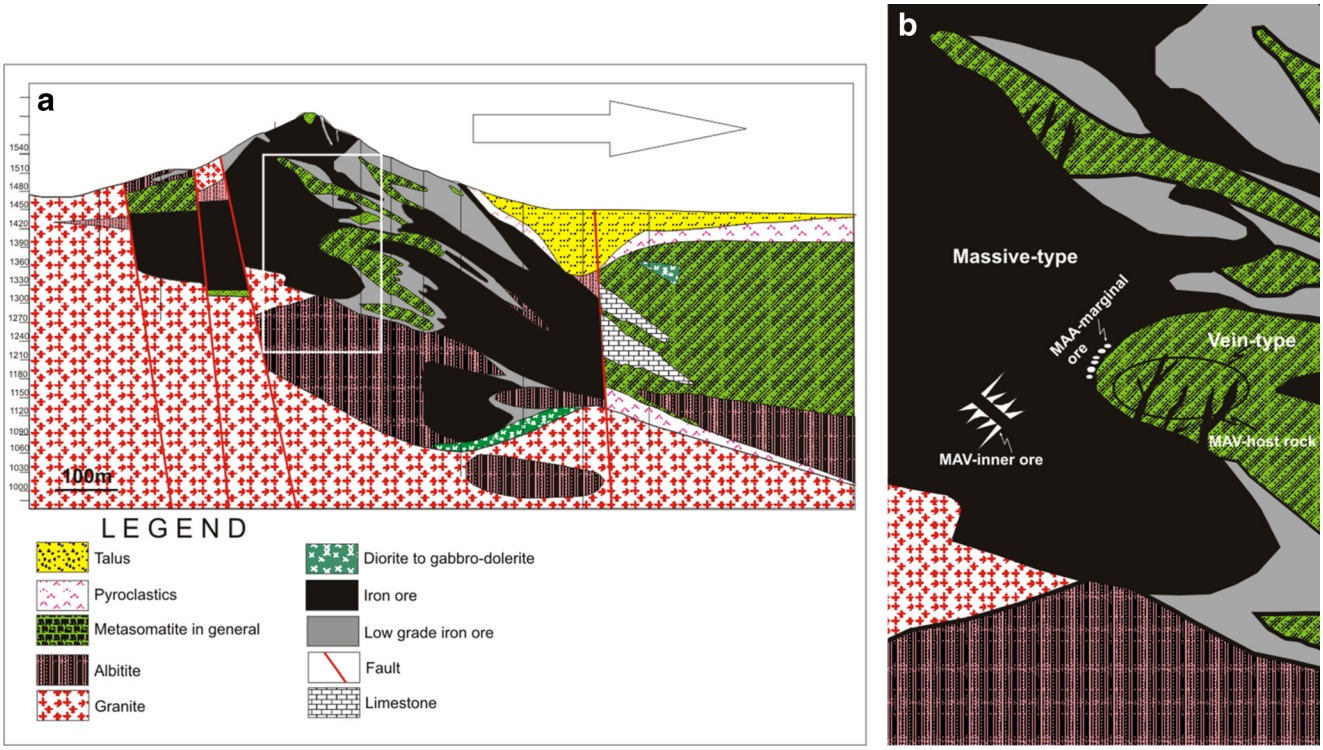

Fig. 2 **a** Geological cross section illustrating field relationship of various alteration types and associated mineralization in Chadormalu **b** a sketch showing the formational environments of magnetite in the deposit (KaniKavan Sharq 2003, 2005 modified after Förster and Jafarzadeh 1983) from the main north bodies

with irregular apatite veinlets from internal part of the main ore body (classified as MAV-inner ore).

The abundance of apatite in Chadormalu and other iron oxide ores from the Bafq district are consistent with their classification as magnetite-apatite ore deposits. Apatite in Chadormalu occurs as apatite-magnetite veins cutting the altered rocks (Fig. 3a, b), disseminated grains and grain aggregates mainly in the marginal parts of the main ore body (Fig. 3 c, d), as well as irregular apatite veinlets in the internal parts of the main ore body (Fig. 3e, f) (Heidarian 2013; Heidarian et al. in review).

Sample material and experiment

In this study, eight samples representing various types of iron ores were selected for detailed ore microscopy, scanning electron microscopy (SEM), and electron probe microanalysis (EPMA). The samples are from three different magnetite-apatite assemblages: a) magnetite-apatite veins in the altered host rocks (four samples: Cha2–1, Cha2–2, Cha8, Ch15) and hereafter named as MAV-host rock; b) magnetite crystals associated with disseminated apatite grains and patches in the marginal parts of the main ore body (two samples: Cha1–1, Cha1–2) and hereafter classified as MAA-marginal ore; c) massive magnetite associated with apatite veinlets in the internal parts of the main magnetite ore bodies (two samples: Cha24–1, Cha24–2) and classified hereafter as MAV-inner ore (Figs. 3 and 4). The approximate locations of the samples are shown in Fig. 4. All samples were studied by optical microscopy to identify the mineralogical and textural relationships. In order to investigate the different textural evidence in detail, the samples were studied by scanning electron microscopy (SEM). Electron probe microanalysis (EPMA) also was utilized to analyze the different generations of magnetite.

The analyses were performed at the University of New Brunswick (UNB), Canada, Microscopy and Microanalysis Facility using JEOL JXA-733 Superprobe Microanalyser, equipped with 4 wavelength-dispersive spectrometers. The data were collected using 1 μm beam diameter at accelerating voltage of 20 kV, and a probe current of 150 nA. The following reference minerals are used: Fe_3O_4 (Fe), $Mg_3Al_2Si_3O_{12}$ (Mg, Al and Si), $(Mn,Ca)SiO_3$ (Ca and Mn), $ZnAl_2O_4$ (Zn), $FeTiO_3$ (Ti), $FeCr_2O_4$ (Cr), vanadium metal (V), cobalt metal (Co) and NiO (Ni).

Results

Microtextures of magnetites

Here the microscopic features of magnetite from the main three ore types are discussed. In the MAV-host rock ore, magnetites occurs in two main generations and are associated with

Fig. 3 Photographs of hand specimens representing various magnetite-apatite associations in Chadormalu. **a, b** magnetite-apatite veins in altered host (MAV-host rock) **c**, **d** magnetites associated with monomineralic apatite patches in the marginal parts of the main ore body (MAA-marginal ore); **e, f** magnetite associated with apatite veinlets in the main ore body (MAV-inner ore)

apatite, calcite, quartz, and actinolite. The primary magnetite (Mag1) displays some oscillatory zoning (SEM-BSE image of average atomic number contrast) consisting of dark (Mag1–1) and light (Mag1–2) bands (Fig. 5a-c). Secondary magnetite (Mag2) is present as irregular patches enclosing or penetrating the primary phase through fractures (Fig. 5a, c, d, f). Recrystallization with well-developed foam-like triple

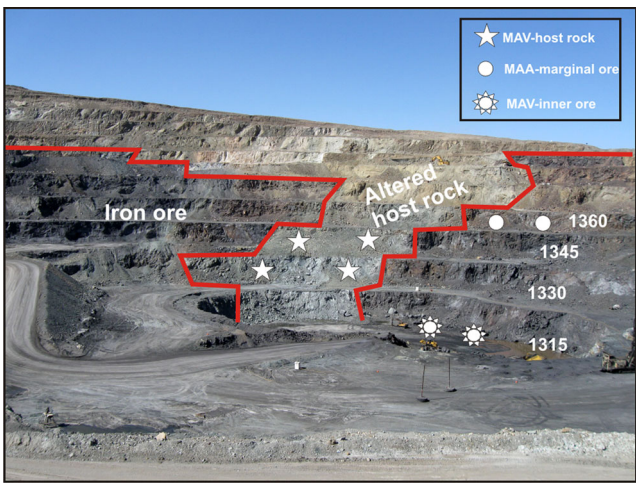

Fig. 4 Photograph showing the north iron ore bodies with the view of northwest in Chadormalu deposit

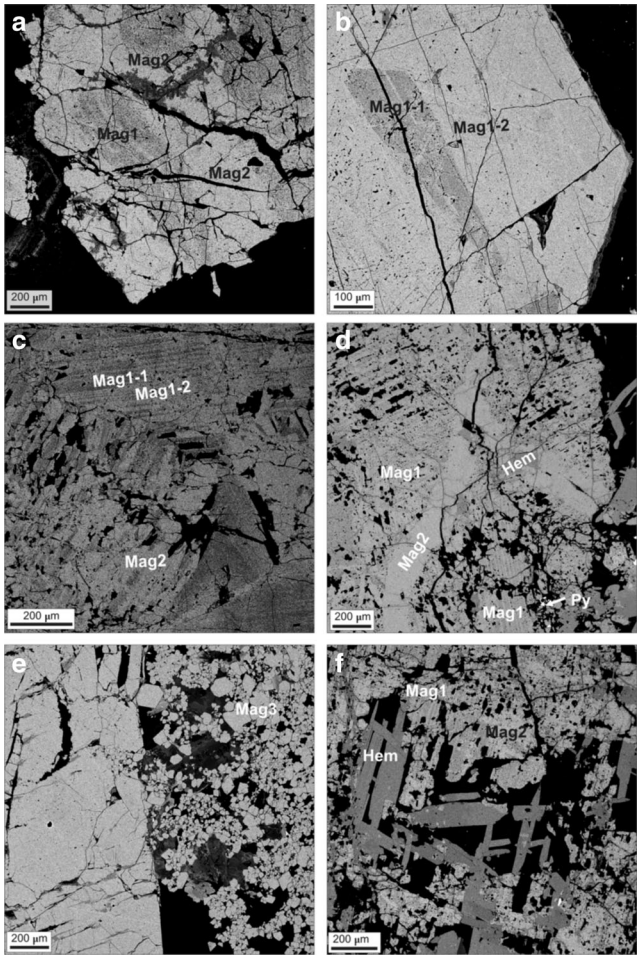

Fig. 5 SEM-backscattered electron (SEM-BSE) images of magnetite from the MAV-host rock ore. **a, b, c** primary magnetite (Mag1) consisting of dark (Mag1–1) and light (Mag1–2) bands. **a, c, d** replacement of the primary magnetite (Mag1) by secondary magnetite (Mag2) as irregular bands and patches. **e** foam-like magnetite with well-developed triple junctions (Mag3) formed through recrystallization of the primary magnetite (Mag1). **f** tabular and needle-shaped hematite grains replacing primary and secondary magnetites. Mineral abbreviations: Mag = magnetite, Hem = hematite, Ap = apatite, Py = pyrite

junctions also occurs in some parts of the sample and is classified as Mag3 (Fig. 5e). Hematite occurs as tabular (needle-shaped/acicular in 2D) crystals, as well as irregular patches replacing both primary and secondary magnetites along their rims and along fractures (Fig. 5d, f).

In the MAA-marginal ore, magnetite grains are in equilibrium with apatite, calcite, quartz, actinolite, and primary hematite (tabular and needle-shaped). Secondary hematite (and goethite), as well as some calcite and secondary quartz, have also been observed in these samples (Fig. 6a). Pyrite crystals are developed as euhedral and well-formed crystals in fractures and cracks in the magnetite grains (Fig. 6b). Similarly, magnetite occurs as two main primary and secondary generations. The Mag1 magnetite crystals have porous and dark appearance in the SEM-BSE images, presumably reflecting lower Fe contents (Fig. 6a-d). Secondary magnetite (Mag2)

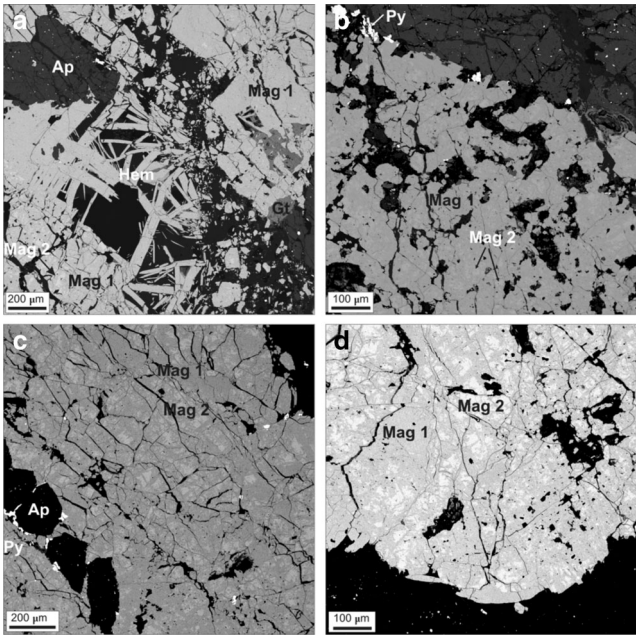

Fig. 6 SEM-backscattered electron (SEM-BSE) images of magnetite grains from MAA-marginal ore. **a-d** primary magnetite (Mag1) replaced by secondary phase (Mag2) due to subsequent alteration. Primary magnetites have dark and porous appearance, whereas secondary magnetites which irregularly replaced primary ones are bright. Hematite in **a** occurring both as needles (plates) and irregular grains on the primary and secondary magnetite. Pyrite crystals formed in fractures cutting former magnetite assemblages

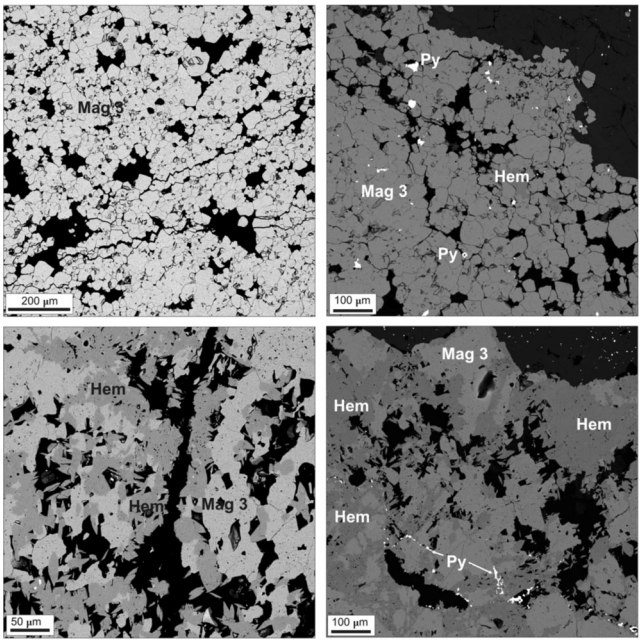

Fig. 7 SEM-backscattered electron (SEM-BSE) images of magnetite grains from MAV-inner ore. **a, b** Recrystallized foam-like magnetite (Mag3) with well-formed triple junctions. **c, d** Needle-shaped and tabular hematite grains formed on the magnetites

mainly occurs as irregular lighter patches replacing primary type (Fig. 6c, d). The light appearance in SEM-BSE images (atomic number contrast) of this type may reflect lower trace element concentrations and higher Fe contents.

The MAV-inner ore only has minor abundances of other paragenetically associated minerals. In this type, magnetite crystals are predominantly recrystallized and appear as euhedral grains (Mag3) with foam-like triple junctions, which formed due to recrystallization of the primary and secondary magnetite (Fig. 7a, b). Hematite occurs as both euhedral crystals and irregular anhedral grains replacing earlier magnetite grains on irregular fractures (Fig. 7c). Like the above magnetite-apatite association, euhedral pyrite crystals appear on or replacing magnetite 3 (Fig. 7d).

Trace element systematics

EPMA results from various magnetite types are presented in Tables 1, 2, and 3. Figure 8 shows comparative box-plot diagrams of different trace elements from magnetite generations in various magnetite types. Primary magnetites (Mag1) from MAV-host rocks (Table 1) contain oscillatory zoning with light and dark bands. The dark bands have lower FeO (89.34–93.29 wt.%; ave. 91.65 wt.%), relatively high SiO_2 (0.033–2.26 wt.%; ave. 0.763 wt.%), Al_2O_3 (0.002–0.452 wt.%; ave. 0.087 wt.%), MgO (0.003–0.94 wt.%; ave. 0.252 wt.%), and moderate TiO_2 (0–1.233 wt.%; ave. 0.325 wt.%), whereas the light-contrast growth zones, typically developed in the primary magnetite (Fig. 5b), show significant differences in trace element composition: the light zones have high FeO (91.53 to 93.65 wt.%; ave. 92.66 wt.%), low to moderate SiO_2 (0.03–0.253 wt.%; ave. 0.074 wt.%), low Al_2O_3 (0.004–0.026 wt.%; average 0.013 wt.%), MgO (0.004–0.070 wt.%; average 0.013 wt.%), and TiO_2 (0–0.950 wt.%; ave. 0.315 wt.%). The secondary magnetite crystals (Mag2) in these assemblages contain high FeO (91.7–93.49 wt.%; ave. 92.86 wt.%), moderate TiO_2 (0.011 to 1.187 wt.%; ave. 0.357 wt.%), and V_2O_3 (0.273–0.343 wt.%; ave. 0.302 wt.%), and lower SiO_2 (0.032–0.098 wt.%; ave. 0.061 wt.%), Al_2O_3 (0.004–0.052 wt.%; ave. 0.01 wt.%), CaO (0–0.034 wt.%; ave. 0.012 wt.%), and MnO (0.010–0.061 wt.%; ave. 0.038 wt.%). Other trace elements, such as CoO, Cr_2O_3, and MgO, are uniformly low, but consistently higher than their respective detection limits.

Mag1 from MAA-marginal ore (Table 2) contain low to moderate FeO contents (88.77 to 93.35 wt.%; ave. 90.20 wt.%) and low to moderate contents of TiO_2 (0–0.715 wt.%; ave. 0.209 wt.%) and V_2O_3 (0.273–0.508 wt.%; ave. 0.326 wt.%), with SiO_2 (0.021–0.226 wt.%; ave. 0.13 wt.%), CaO (0.011–0.119 wt.%; ave. 0.061 wt.%), MnO (0–0.038 wt.%; ave. 0.019 wt.%) and Al_2O_3 (0.016–0.167 wt.%; ave. 0.061 wt.%). Other elements including Cr_2O_3, ZnO, NiO, and MgO are higher than their detection limit. Mag2 also have higher FeO contents (89.23 to 92.95 wt.%; ave. 91.37 wt.%), low to moderate TiO_2 (0–

Table 1 Representative results of EMPA of magnetites from MAV-host rock

Sample	Cha2–1		Cha2–2						Cha8		Cha15										
Gen.	Mag1–2	Mag2	Mag1–1	Mag1–1	Mag2	Mag2	Mag1–2	Mag1–2	Mag1–2	Mag1–1	Mag1–1	Mag1–1	Mag1–2	Mag1–2	Mag1–1	Mag1–1	Mag2	Mag2	Mag2	Mag2	Mag2
MgO	0.020	0.012	0.006	0.197	0.004	0.025	0.007	0.070	0.004	0.003	0.940	0.006	0.004	0.018	0.363	0.006	0.005	0.006	0.066	0.004	0.005
Al_2O_3	0.010	0.004	0.002	0.031	0.013	0.006	0.007	0.026	0.023	0.012	0.235	0.004	0.004	0.022	0.452	0.057	0.009	0.013	0.052	0.015	0.012
SiO_2	0.090	0.066	0.042	0.564	0.032	0.084	0.062	0.253	0.031	0.033	2.260	0.048	0.109	0.105	1.518	0.035	0.075	0.060	0.098	0.056	0.042
CaO	0.035	0.025	0.241	0.096	0.000	0.012	0.008	0.050	0.001	0.055	0.481	0.053	0.022	0.014	0.283	0.002	0.024	0.007	0.013	0.020	0.034
TiO_2	0.048	0.149	0.154	0.014	0.680	0.088	0.187	0.215	0.386	0.432	0.032	0.004	0.000	0.950	0.618	1.233	0.023	1.187	0.011	0.075	0.585
V_2O_3	0.283	0.284	0.275	0.249	0.345	0.275	0.310	0.306	0.355	0.318	0.281	0.289	0.285	0.374	0.373	0.409	0.289	0.343	0.283	0.273	0.307
Cr_2O_3	0.016	0.014	0.013	0.017	0.018	0.017	0.021	0.017	0.025	0.018	0.017	0.017	0.019	0.016	0.033	0.162	0.017	0.018	0.018	0.017	0.020
MnO	0.017	0.016	0.017	0.016	0.013	0.010	0.027	0.017	0.054	0.090	0.061	0.054	0.044	0.028	0.066	0.051	0.053	0.061	0.046	0.058	0.057
FeO	91.53	91.70	92.72	90.97	92.78	92.24	92.87	92.38	92.62	92.40	89.34	93.29	93.65	89.34	91.91	92.43	93.49	92.29	93.16	93.20	93.34
CoO	0.096	0.101	0.094	0.091	0.104	0.098	0.103	0.107	0.104	0.098	0.098	0.110	0.106	0.098	0.097	0.106	0.104	0.109	0.107	0.111	0.100
NiO	0.022	0.019	0.012	0.016	0.009	0.013	0.015	0.015	0.022	0.004	0.008	0.004	0.014	0.008	0.005	0.014	0.008	0.007	0.016	0.003	0.007
ZnO	0.000	0.000	0.000	0.000	0.000	0.000	0.000	0.000	0.000	0.000	0.000	0.000	0.000	0.000	0.000	0.000	0.000	0.000	0.000	0.000	0.000
Total	92.170	92.390	93.570	92.260	94.000	92.870	93.610	93.450	93.620	93.460	93.761	93.880	94.260	94.370	93.540	94.510	94.090	94.100	93.870	93.830	94.510

Detection limits are 0.002 (Mg, Al, Si, Ca), 0.003 (Ti, V, Cr), 0.007 (Mn), 0.019 (Fe), 0.009 (Co, Ni, Zn)

Gen: generation

Table 2 Representative results of EMPA of magnetites from MAA-marginal ore

Sample	Cha1–1											Cha1–2						
Gen.	Mag1	Mag1	Mag1	Mag1	Mag1	Mag1	Mag2	Mag2	Mag2	Mag2	Mag2	Mag2	Mag2	Mag2	Mag2	Mag1	Mag2	Mag1
MgO	0.000	0.066	0.019	0.001	0.000	0.010	0.003	0.001	0.018	0.004	0.000	0.012	0.003	0.003	0.004	0.000	0.001	0.066
Al_2O_3	0.035	0.167	0.126	0.032	0.113	0.025	0.024	0.032	0.046	0.042	0.025	0.031	0.004	0.072	0.014	0.016	0.015	0.109
SiO_2	0.209	0.551	0.116	0.153	0.024	0.226	0.19	0.040	0.068	0.160	0.084	0.205	0.038	0.174	0.067	0.021	0.037	0.074
CaO	0.066	0.082	0.018	0.065	0.011	0.058	0.016	0.008	0.009	0.003	0.053	0.021	0.030	0.009	0.001	0.119	0.003	0.068
TiO_2	0.134	0.440	0.715	0.000	0.287	0.081	0.000	0.235	0.810	0.043	0.263	0.001	0.000	0.188	0.074	0.111	0.113	0.316
V_2O_3	0.273	0.336	0.350	0.309	0.508	0.302	0.307	0.331	0.340	0.280	0.434	0.289	0.231	0.314	0.295	0.330	0.349	0.322
Cr_2O_3	0.014	0.020	0.015	0.019	0.032	0.019	0.016	0.017	0.018	0.018	0.024	0.017	0.014	0.020	0.017	0.018	0.021	0.019
MnO	0.015	0.030	0.021	0.019	0.000	0.029	0.009	0.024	0.028	0.015	0.000	0.021	0.010	0.018	0.008	0.000	0.015	0.038
FeO	93.35	88.77	92.68	88.94	90.15	88.96	89.23	92.95	90.91	89.26	89.66	90.27	92.40	90.41	92.66	89.72	92.58	92.23
CoO	0.104	0.094	0.099	0.085	0.094	0.096	0.099	0.095	0.095	0.107	0.089	0.098	0.094	0.095	0.106	0.088	0.094	0.102
NiO	0.013	0.016	0.021	0.019	0.000	0.018	0.026	0.015	0.013	0.015	0.000	0.016	0.016	0.017	0.020	0.000	0.019	0.019
ZnO	0.000	0.000	0.000	0.000	0.000	0.000	0.000	0.000	0.003	0.000	0.000	0.000	0.000	0.000	0.000	0.002	0.000	0.000
Total	94.210	90.570	94.180	89.640	91.22	89.82	89.92	93.750	92.360	89.950	90.630	90.980	92.840	91.320	93.260	90.430	93.240	93.370

Detection limits are 0.002 (Mg, Al, Si, Ca), 0.003 (Ti, V, Cr), 0.007 (Mn), 0.019 (Fe), 0.009 (Co, Ni, Zn)

Gen: generation

Table 3 Representative results of EMPA analyses of magnetites from MAV-inner ore

Sample	Cha24–1								Cha24–2									
Gen.	Mag3	Mag3	Mag3	Mag3	Mag3	Mag3	Mag3	Mag3	Mag3	Mag3	Mag3	Mag3	Mag3	Mag3	Mag3	Mag3	Mag3	Mag3
MgO	0.002	0.002	0.006	0.000	0.000	0.002	0.005	0.207	0.075	0.000	0.027	0.009	0.012	0.007	0.004	0.005	0.000	0.027
Al_2O_3	0.002	0.033	0.058	0.022	0.732	0.033	0.052	0.219	0.103	0.036	0.021	0.008	0.000	0.007	0.003	0.004	0.000	0.020
SiO_2	0.043	0.045	0.162	0.047	0.062	0.045	0.171	1.445	0.839	0.073	0.054	0.035	0.045	0.040	0.042	0.046	0.062	0.054
CaO	0.001	0.000	0.016	0.073	0.014	0.000	0.007	0.242	0.090	0.065	0.503	0.042	0.102	0.041	0.012	0.017	0.164	0.050
TiO_2	0.197	0.053	0.000	0.063	0.126	0.053	0.003	0.000	0.001	0.000	0.000	0.100	0.024	0.103	0.083	0.090	0.021	0.000
V_2O_3	0.412	0.250	0.284	0.242	0.257	0.250	0.262	0.249	0.262	0.261	0.377	0.405	0.411	0.396	0.394	0.396	0.393	0.377
Cr_2O_3	0.027	0.015	0.016	0.014	0.013	0.015	0.017	0.013	0.014	0.016	0.025	0.026	0.025	0.026	0.026	0.027	0.032	0.025
MnO	0.016	0.010	0.001	0.003	0.001	0.01	0.004	0.010	0.000	0.009	0.022	0.029	0.032	0.024	0.025	0.023	0.019	0.022
FeO	92.93	93.80	93.58	93.33	92.94	93.8	93.52	91.73	92.7	93.16	91.25	92.99	92.95	93.50	93.25	93.44	91.81	91.25
CoO	0.099	0.101	0.099	0.099	0.095	0.101	0.104	0.099	0.101	0.094	0.105	0.103	0.097	0.104	0.108	0.094	0.089	0.105
NiO	0.015	0.024	0.020	0.029	0.018	0.024	0.024	0.016	0.023	0.021	0.021	0.019	0.016	0.025	0.017	0.021	0.021	0.021
ZnO	0.000	0.000	0.000	0.000	0.000	0.000	0.000	0.000	0.000	0.000	0.000	0.000	0.000	0.003	0.000	0.000	0.005	0.000
Total	93.75	94.33	94.24	93.92	94.25	94.33	94.17	94.23	94.21	93.73	92.41	93.76	93.71	94.28	93.96	94.16	92.62	92.41

Detection limits are 0.002 (Mg, Al, Si, Ca), 0.003 (Ti, V, Cr), 0.007 (Mn), 0.019 (Fe), 0.009 (Co, Ni, Zn)

Gen: generation

0.810 wt.%; ave. 0.169 wt.%) and V_2O_3 (0.280–0.434 wt.%; average 0.310 wt.%) and lower SiO_2 (0.037–0.205 wt.%; average 0.084 wt.%), Al_2O_3 (0.004–0.072 wt.%; ave. 0.029), and CaO (0.001–0.053 wt.%; ave. 0.015 wt.%). Other trace elements including MnO, CoO, Cr_2O_3, and MgO are similar to Mag1.

Magnetite crystals in MAV-inner ore (Table 3) (Mag3), which have recrystallized texture contain high FeO (91.25–93.8 wt.%; ave. 92.69 wt.%), low TiO_2 (0–0.197 wt.%.; ave. 0.058 wt.%), and MnO (0–0.034 wt.%; ave. 0.017 wt.%) and moderate V_2O_3 (0.242–0.473 wt.%; ave. 0.357 wt.%) with low to high contents of SiO_2 (0.008–1.445 wt.%; ave. 0.131 wt.%), Al_2O_3 (0–0.732 wt.%; ave. 0.059 wt.%) and CaO (0–0.503 wt.%; ave. 0.072 wt.%). Other trace elements, such as CoO, Cr_2O_3, and MgO, have low concentrations.

Discussion

Generalities

According to spatial distribution and textural features of magnetite from different magnetite-apatite associations, three main magnetite generations (Mag1, Mag2, and Mag3) can be distinguished in the Chadormalu iron deposit (Figs. 5, 6, 7, 9). Primary magnetites developed during the first episode of magnetite mineralization, have darker SEM-BSE contrast and have a porous appearance (Fig. 9a1, b1). Porous appearance of magnetite in similar deposits has been discussed as a result of dissolution processes which might be related to the environment of formation (Hu et al. 2014; Makvandi et al. 2015). The secondary magnetites (Mag2) show replacive sharp, irregular contacts with lighter appearance than primary ones (Fig. 9a2, b2). According to the composition of the different magnetite types, it is obvious that the primary varieties have relatively higher concentrations of SiO_2, Al_2O_3, and CaO than secondary varieties. These features are interpreted to be the result of lateral alteration processes known as dissolution and precipitation (Hu et al. 2014 and references therein; Makvandi et al. 2015). Low to moderate Ti and V contents of the primary magnetites cannot be related to magmatic or porphyry systems (c.f. Nadoll et al. 2014). It can be inferred from moderate contents of SiO_2 and Al_2O_3 of primary magnetite that they were crystallized from magmatic-dominated hydrothermal fluids evolving similar to those in IOCG and Kiruna type deposits (Fig. 9d). The oscillatory zoning that has been observed only in the magnetite-apatite veins crosscutting the altered host rocks (Figs. 5a-e, 9a1), formed due to fluctuating Fe solubility and therefore changing the iron saturation level in the ore-forming fluid, which might be magmatic dominated with moderate Al and Si (Hu et al. 2014). Dare et al. (2014) noted that these zonation patterns could be related to varying fluid composition and different physico-chemical parameters,

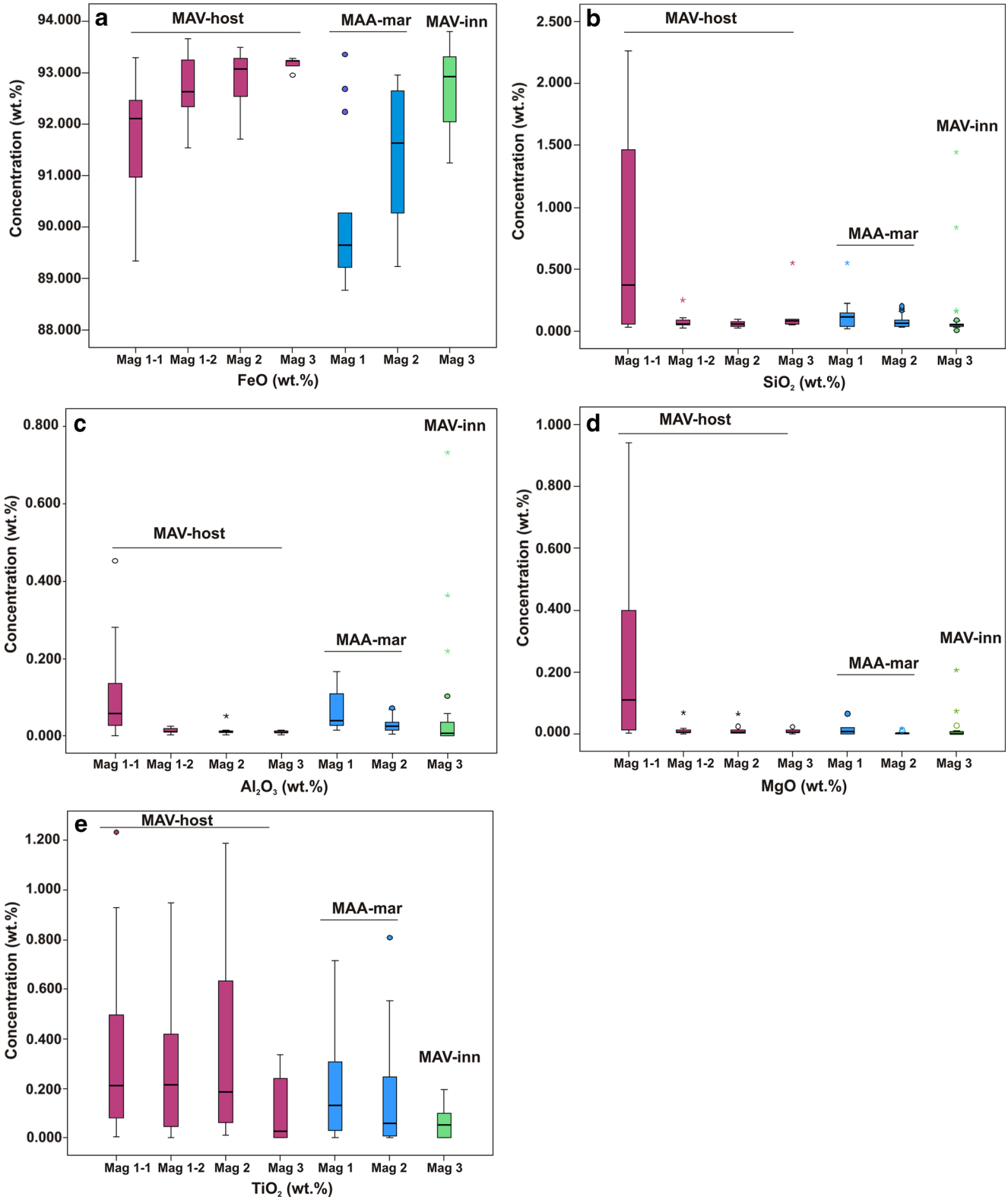

Fig. 8 **a-e** Comparative box-plot diagrams for various trace elements from magnetite generations in different magnetite types of Chadormalu deposit

including temperature, pH, and perhaps redox conditions, which change the partitioning behavior of trace elements into magnetite during its growth.

The porous primary phase was then largely replaced by secondary magnetites (Mag2), which preferentially occur along microfractures and grain boundaries of primary

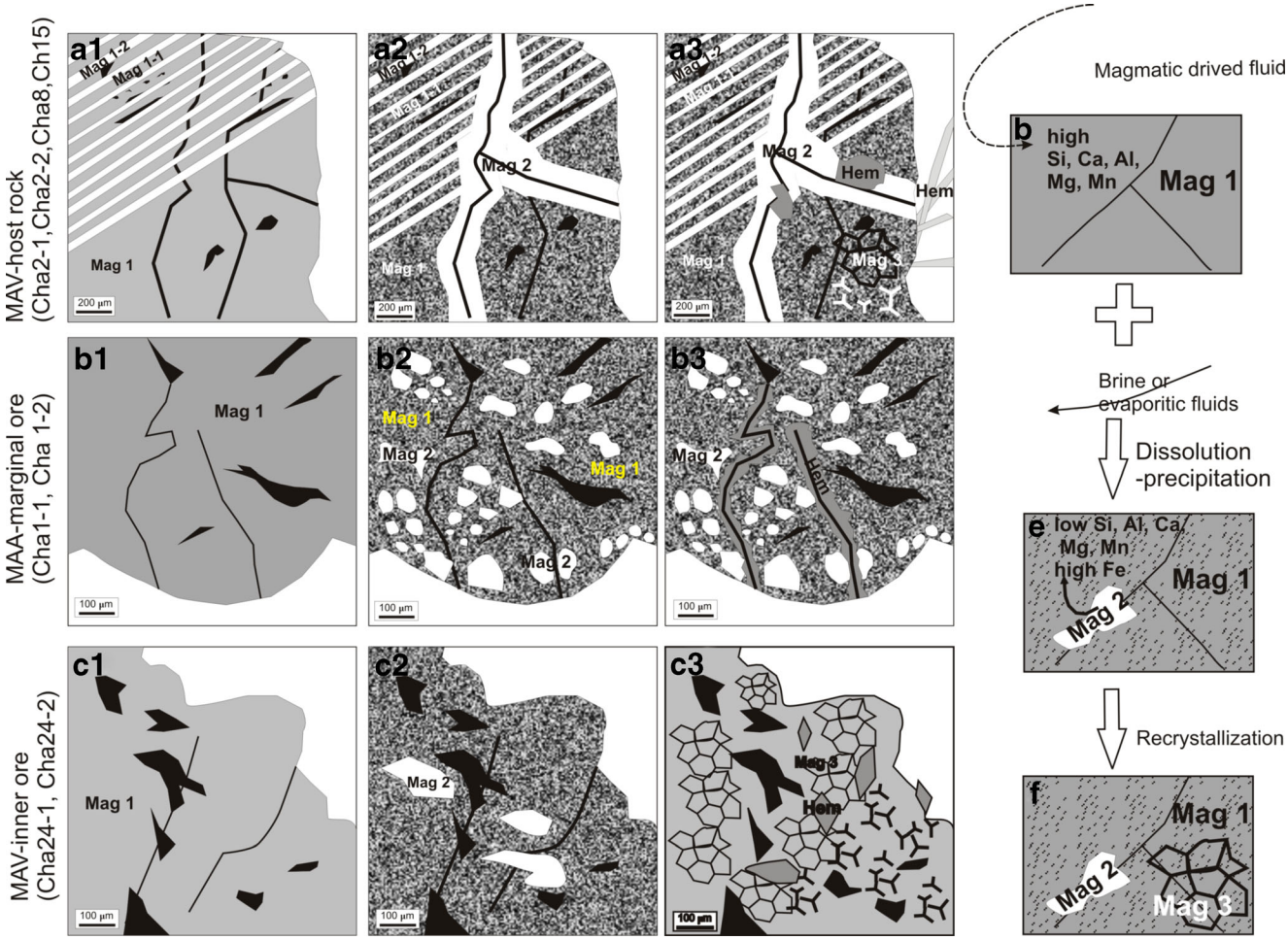

Fig. 9 Schematic illustrations displaying different stages of magnetite formation in Chadormalu magnetite deposit. **a1-a3** primary (Mag1), secondary (Mag2) and recrystallized magnetite (Mag 3) in the MAV-host rock ore. **b1-b3** primary (Mag1) and secondary magnetites (Mag2) in MAA-marginal ore. **b3** hematite crystallization on magnetite from MAA-marginal ore. **c1-c3** various magnetite generations (Mag1, Mag2, Mag3) in the MAV-inner ore. **d** magmatic-derived hydrothermal fluids assisted in the formation of the primary magnetites (Mag1), while in **e** evaporitic fluids or brines have influenced Mag1 by dissolution-precipitation to form replacive secondary magnetites (Mag2). **f** recrystallization processes that occurred in some parts of the Chadormalu deposit, including MAV-inner ore and partly in MAV-host rock

magnetites (Fig. 9a2, b2). Dissolution of primary phase can increase permeability and facilitates infiltration of fluids (Makvandi et al. 2015). Development of dissolution may create some irregular cracks and microfractures in the primary phase, which results in volume loss in the replacement reactions (Larson 1983; Deo et al. 1989; Boucher et al. 2010). The overgrowth of secondary magnetites (Mag2) on Mag1 might be due to supersaturation of ore fluids which results in precipitation of new magnetite crystals (Makvandi et al. 2015). These replacement reactions were facilitated by a hydrothermal fluid due to dissolution of primary magnetites (Mag1) and direct precipitation of a secondary variety (Hu et al. 2014; Makvandi et al. 2015) (Mag2; Fig. 9e). During this reaction, Si, Al, and Ca were removed from the primary variety.

Different parameters can affect the dissolution and precipitation reactions including: the fluid phase composition, solubility of mineral phases, temperature and pressure, Eh and pH stability fields of magnetites, and oxygen and sulfur fugacities (Putnis 2002; Putnis and Putnis 2007; Xia et al. 2009; Putnis and John 2010; Pollok et al. 2011; Jonas et al. 2013; Borg et al. 2014; Makvandi et al. 2015). According to Hu et al. (2014) and references therein, the higher contents of low ionic radius cations, including Si^{4+}, make the magnetites more susceptible to fluid-assisted alteration.

Infiltration of mixed basinal brine and meteoric waters that already dissolved evaporates can be an important component in changing the physico-chemical parameters of ore-forming fluids, which led to replacement reactions that formed secondary magnetites (Mag2) (Fig. 9e). These high salinity ore-forming fluids enhance Fe solubility and lead disequilibrium between primary magnetites and evolving surficial fluids (Whitney et al. 1985; Hemley and Hunt 1992). The Rizu and Dezu formations in Bafq district might be the evaporitic source for the brine contribution to the hydrothermal system

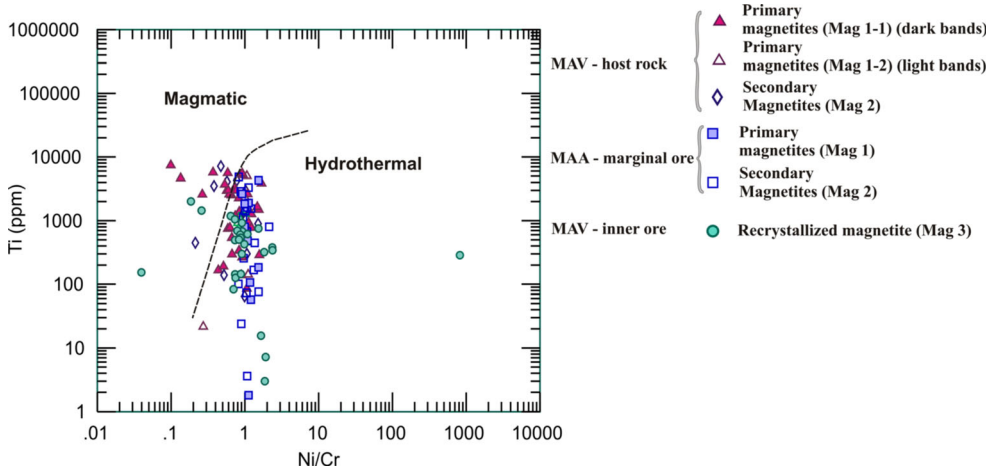

Fig. 10 Plot of Ti versus Ni/Cr ratio from Chadormalu different magnetite types. The fields are from Dare et al. (2014) and references therein

that is reflected in alteration of enclosing host rocks (Ramezani and Tucker 2003; Heidarian 2013; Heidarian et al. in review).

This reequilibration may result in some porosity development in primary magnetite crystals, which further promotes precipitation of new magnetite phases (Hu et al. 2014 and references therein; Makvandi et al. 2015). Some magnetite-apatite veins, including those hosted in altered host rocks and in the main ore body, display well-defined 120° triple junctions (foam texture), and fine recrystallized grains (Figs. 5g, 9a3). There are several interpretations for the origin of foam texture, such as magmatic, metamorphic, and metasomatic events (Nold et al. 2013). Förster and Jafarzadeh (1994) and Mücke and Younessi (1994) reported similar fabrics from the Chahgaz iron ore deposit (Bafq district) and Gol-Gohar deposit (southern Sanandaj-Sirjan belt, Iran), respectively, and interpreted that as a result of magmatic processes. However, Daliran et al. (2010) suggested a metasomatic origin for the foam texture in the Bafq district iron ore deposits. Hu et al. (2015) proposed two models for this textural feature:

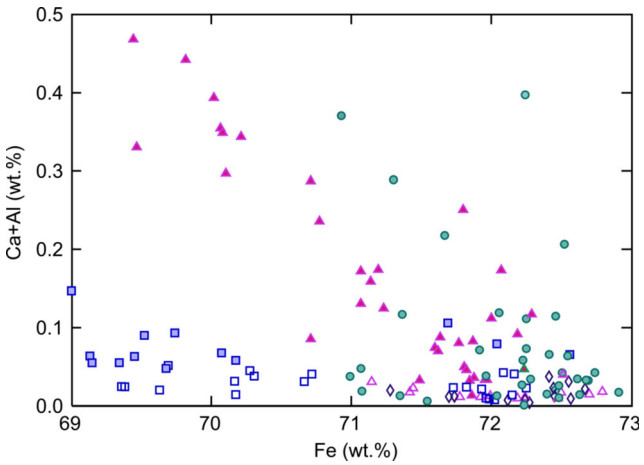

Fig. 11 Ca + Al vs. Fe diagram of primary (Mag1) and secondary (Mag2) magnetite from different magnetite-apatite types showing. The symbols are the same as in Fig. 10

recrystallization or annealing due to higher temperature in the deformation zone (i.e., magnetite; Ciobanu and Cook 2004), and replacement of minerals by the fluids in an open system (i.e., quartz; Nakamura and Watson 2001). However, Mücke and Younessi (1994) suggested a magmatic origin for this texture and discussed that as a crystallization product of magma. In magnetite-apatite assemblages in the Chadormalu main ore body, magnetite grains have foam-like triple junctions (Figs. 7a, b, 9c2, c3) and show different chemical patterns, which cannot be related to a recrystallization process at high temperature conditions such as magmatic or metamorphic environments (c.f. Hu et al. 2015). Therefore, these recrystallized magnetites likely resulted from a fluid replacement process in a metasomatic environment (Fig. 7f).

Mechanisms controlling the trace element composition of magnetite

The geochemical composition of hydrothermal magnetite may be controlled by different factors: 1) composition of ore fluids; 2) composition of host rocks which already reacted with fluids; and 3) physicochemical parameters of ore forming fluids, such as P, T, oxygen and sulfur fugacity (Dare et al. 2014; Nadoll et al. 2014). Different trace element compositions of primary and secondary magnetites indicate that they formed via different mechanisms. Relatively low Ti (<2 wt.%) and Al (<1 wt.%) are representative of hydrothermal deposits (Nadoll et al. 2014), because of their lower activity in magmatic-derived fluids (Ray and Webster 2007; Dupuis and Beaudoin 2011; Nadoll et al. 2012, 2014). As mentioned above, different magnetite-apatite types in Chadormalu deposit show lower Al and Ti contents, which is consistent with hydrothermal genesis. Other important indicator elements, Ni and Cr, mostly decouple magmatic from hydrothermal magnetite paragenesis (see Dare et al. 2014). In many hydrothermal settings, the Ni/Cr ratio is typically higher (≥1), probably due to a greater solubility and availability of Ni compared

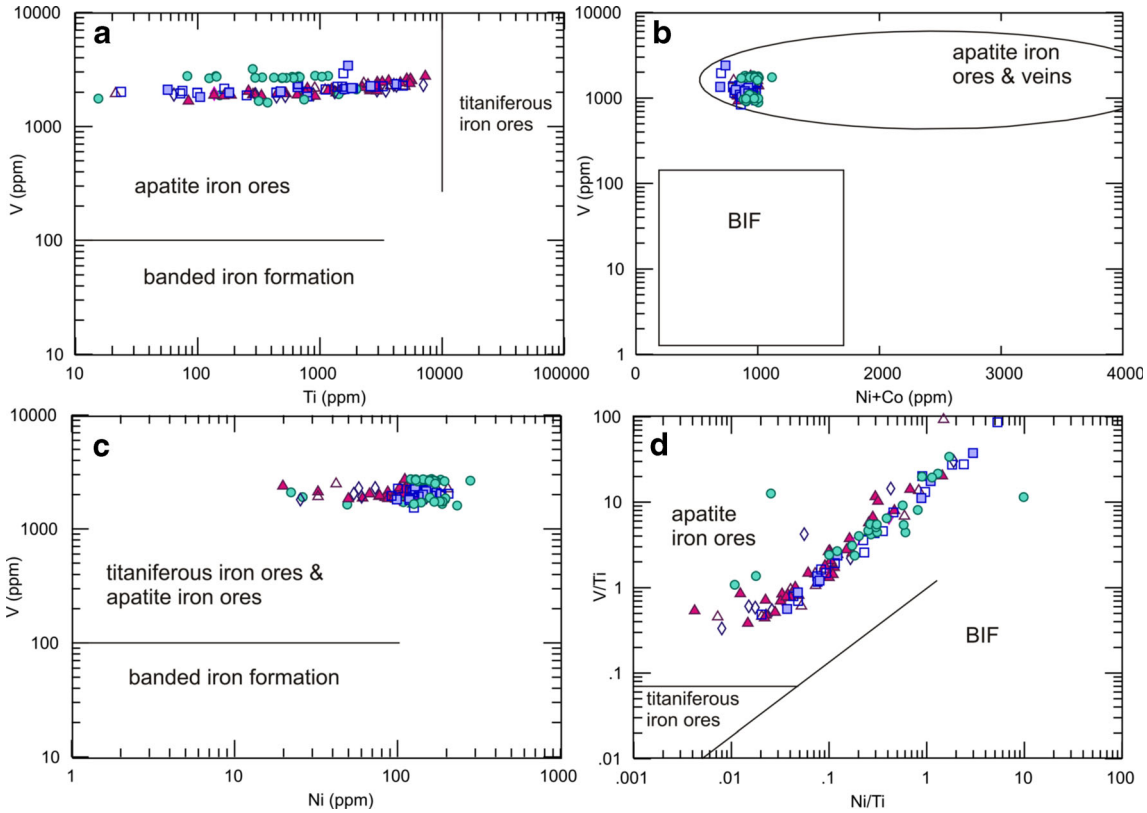

Fig. 12 **a-d** Ferride elements (Fe, Ni, V, Ti) of Chadormalu magnetites plottes on Lohberg and Horndhal (1983) diagrams. The symbols are the same as in Fig. 10

to Cr in fluids. The plot of Ti vs. Ni/Cr (Fig. 10) is used to discriminate between magnetite from hydrothermal versus all magmatic igneous environments. According to Fig. 10, the various magnetite types mostly plot in the hydrothermal magnetite field. However, some primary magnetites, including those from MAV-host rock fall in the magmatic field, which can be representative of contribution from magmatic dominated fluids in the magnetite formation.

However, it is obvious that primary magnetites have relatively higher contents of Si, Al, Ca, and Mg, which might be related to a major contribution of magmatic-derived fluids due to large fluid-rock ratios at the site of mineral deposition (c.f. Dupuis and Beaudoin 2011; Nadoll et al. 2012, 2014; Dare et al. 2014), especially from the MAV-host rock. Further dilution of magmatic hydrothermal fluids and increased infiltration of surficial brines led to formation of secondary magnetite with lower Si, Al, Ca, and Mg contents replacing primary types. Consistently, the FeOt contents of secondary varieties of magnetite increased up to 93.50 wt.% (Tables 1, 2 and 3). Therefore, it can be concluded that secondary magnetites formed via a process of replacing primary types, due to a dissolution process that resolved Fe from the Mag1, leading to supersaturation and precipitation of new magnetite crystals as Mag2 (c.f. Makvandi et al. 2015). High salinity magmatic fluids or later infiltrating brines could be responsible for the dissolution and precipitation processes. Hu et al. (2014) mentioned this process as an important enrichment mechanism for hydrothermal iron deposits.

In addition, in this deposit, the host rock composition had an important control on the hydrothermal magnetite, particularly for those formed in the metasomatized rocks (see Dare et al. 2014). In Chadormalu, magnetite from the MAV-host rocks show higher Ca and Al contents (Fig. 11). It is obvious in Fig. 11 that different magnetite-apatite assemblages show various trends in Ca + Al vs. Fe, which might be related to their host rocks. Magnetite-apatite veins in the altered host rocks show a negative trend in which the primary magnetites (Mag1) have higher contents of Ca and Al. These can be explained by host rock controls on the composition of magnetite. However, MAA-marginal ore show lower Ca and Al contents with a wide variety of Fe contents. Disseminated magnetite-apatite assemblages in the main ore body (MAA-marginal ore) have low Ca contents and can be divided into a higher Fe magnetite which compositionally overlaps with secondary types (Mag2), and a lower Fe magnetite consisting of primary ones having slightly higher Ca contents. Magnetite associated with apatite veinlets (MAV-inner ore) in the main ore body distinctly show higher contents of Fe. Therefore, it can be concluded that host rocks, as well as the hydrothermal fluid, had an important impact on the trace element

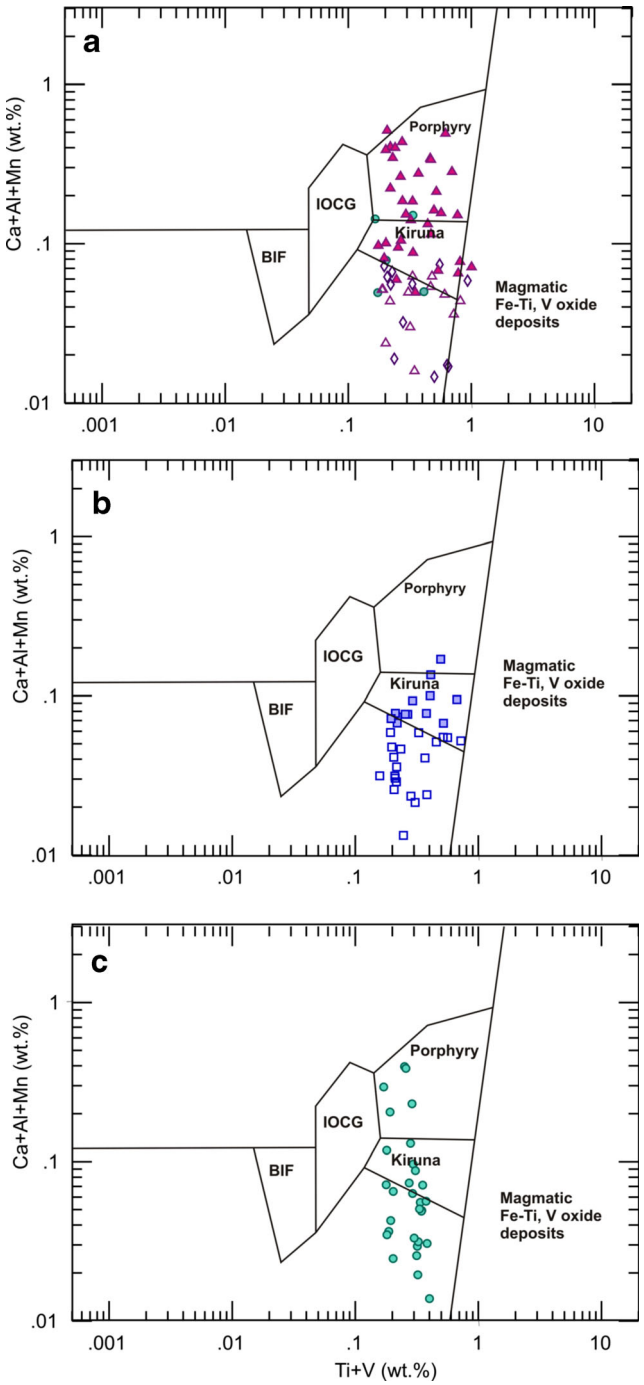

Fig. 13 **a, b, c** Plot of Ti + V vs. Ca + Al + Mn for magnetite from different magnetite-apatite associations in the Chadormalu iron deposit. The reference fields are from Dupuis and Beaudoin (2011). BIF = banded iron formation, Skarn = Fe\Cu skarn deposits, IOCG = iron oxide–copper–gold deposits, Porphyry = porphyry Cu deposits, Kiruna = Kiruna apatite–magnetite deposits, Fe\Ti, V = magmatic Fe\Ti\V-oxide deposits. The symbols are the same as in Fig. 10

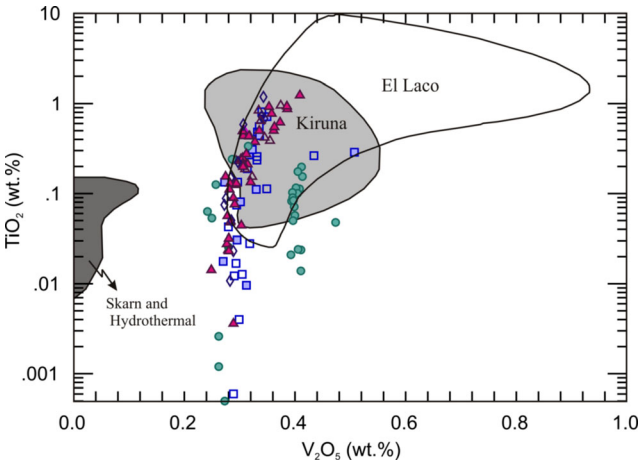

Fig. 14 Plot of V_2O_5 vs. TiO_2 (wt.%) for magnetite from different magnetite-apatite associations in the Chadormalu iron deposit. Various magnetites plot in the Kiruna or El Laco fields. The magnetites from MAV-inner ore show higher contents of V_2O_5. The reference areas are from Hu et al. (2014). The symbols are the same as in Fig. 10

composition specially (Ca and Al contents) of different magnetite types within the Chadormalu deposit. Sequential fluid reaction and interactions with altered host rocks might have changed the trace element composition of fluids that were responsible for magnetite. The higher Al and Ca contents of magnetites from the internal parts of the main ore body can be result of interaction with the altered host rock.

Trace element compositions and implications for the ore genesis

The genesis of Kiruna iron oxide deposits is still quite a controversial argument. A magmatic-hydrothermal replacement (Sillitoe and Burrows 2002), liquid immiscibility (Nyström and Henriquez 1994; Naslund et al. 2002) and hydrothermal precipitation (Barton 2014) have been invoked for the formation of these magnetite deposits. Knipping et al. (2015), provide evidence that giant Kiruna type deposits, such as Los Colorados (LC) in northern Chile, form through efficient flotation of magmatic magnetite suspensions.

The Bafq district iron deposits have been extensively described and discussed; the genesis of deposits, however, has long been a matter of debate. Förster and Jafarzadeh (1994) proposed an immiscible liquid magmatic model for the magnetite-apatite deposits of the Bafq district. Mücke and Younessi (1994) compared some Bafq Fe deposits with those in the Sanandaj-Sirjan zone of Iran and considered them all to be of magmatic (molten) in origin, based on textural and mineralogical associations. However, Daliran (2002) concluded that hydrothermal fluids had played a significant role in the development of the Bafq iron deposits. Moore and Modabberi (2003) suggested that hydrothermal processes dominated by alkali alteration controlled the formation of the Choghart deposit and possibly other iron deposits in the Bafq district. Jami et al. (2007) and Jami (2005) presented evidence that an evolving hydrothermal system associated with submarine magmatic activity was responsible for the formation of the

Esfordi magnetite-apatite deposit. However, Mohseni and Aftabi (2015) presented evidence which considered central Iranian iron deposits as glaciogenic BIF.

The Chadormalu iron deposit can be compared in many aspects with other IOA deposits in the Bafq district, Iran (Daliran 1990; Mousavi Nasab 1994), as well as the Kiruna deposits of Sweden (Nyström and Henriquez 1994) and the Triassic Yangyang iron-oxide–apatite deposits, South Korea (Seo et al. 2015). On various discrimination diagrams using V, Ti, Ni, and Co elements, the Chadormalu iron ores are distinguished from banded iron ore deposits, and plot in the apatite-bearing iron ore field (Fig. 12) (Lohberg and Horndhal 1983).

Using the Ca + Al + Mn versus Ti + V discrimination diagram (Dupuis and Beaudoin 2011), various magnetite types from Chadormalu deposit plot within or close to the fields defined for the Kiruna- and porphyry-related deposits. Dark bands of primary magnetites (Mag1–1) from magnetite-apatite veins in the host altered rocks plot in both Kiruna and porphyry fields, whereas the light bands from the same ore type (Mag1–2), as well as the secondary magnetites (Mag2), plot below the Kiruna field, because of their lower Ca, Mn, and Al contents (Fig. 13a). According to Fig. 13b, most of the primary magnetites (Mag1) from the magnetite-apatite assemblages in the main ore body plot in the Kiruna field suggesting contribution from magmatic fluids, whereas secondary magnetites (Mag2) have lower amounts of Ca, Mn, and Al, and generally fall below the Kiruna field (Fig. 13b). Magnetite associated with apatite veinlets in the main ore body dispersed within and below the Kiruna to the porphyry fields, and it might not related to homogenization through recrystallization (Mag3) (Fig. 13c). Similarly, magnetite from different magnetite-apatite assemblages plot within the fields defined by Kiruna or El Laco deposits on the TiO_2 vs. V_2O_5 diagram (Fig. 14). It is worth noting that recrystallized magnetite (Mag3) from MAV-inner ore show higher V_2O_5 contents compared to other types (Fig. 14).

Recent fluid inclusion studies on the abundant fluid inclusions from apatite grains coexisting with magnetite show a contribution of low to moderate temperature (208° - 406 °C and 266° - 580 °C for vein-type and massive ore, respectively) and saline fluids (0.33 to 24.43 and 0.49 to 10.74 wt.% NaCl equiv. for vein-type and massive ore, respectively) confirming a hydrothermal fluid contribution in the magnetite formation (Heidarian et al. 2012; Heidarian 2013). The $\delta^{34}S$ values were obtained for several pyrite bearing samples; the calculated $\delta^{34}S$ values for the H_2S fluid, using average homogenization temperatures, are about 10.74 ‰ for massive ore and 18.6 ‰ for vein-type ore, implying an evolving fluid source from magmatic dominated to a ^{34}S enriched sulfur source, which could be related to a basinal brine (Heidarian et al. in review).

Our studies, based on textural and chemical evidence, suggest that iron ore formation in Chadormalu was not a simple process and that several magnetite generations formed in the course of the evolution of the ore-forming fluids. The primary magnetites (Mag 1) in MAV-host rock and MAA-marginal ore, show textural and chemical composition consistent with a higher ratio of magmatic-derived hydrothermal fluid in the early stages of primary magnetite formation, while secondary magnetites were formed under a higher proportion of saline brines. These secondary magnetites show textures related to dissolution-precipitation processes. The trace element compositions of the different magnetite generations from various Chadormalu magnetite-apatite assemblages show that the hydrothermal fluids are similar to those of other Kiruna-type iron ore-forming environments.

Conclusions

Several line of evidence including textural and compositional data from various Chadormalu magnetite-apatite assemblages demonstrated that:

- There are three different magnetite generations formed via various mineralization stages.
- Primary magnetites (Mag 1) showing porous and darker appearance, and containing higher Si, Al, and Ca, formed from contribution of higher proportions of magmatic- derived fluids in a Kiruna-type environment.
- Secondary magnetites (Mag 2) that replaced the first generation of magnetites (Mag 1), have lighter appearance and lower Si, Al, and Ca, and formed via a brine fluid contribution in the hydrothermal ore forming fluid.
- The next magnetite generation (Mag 3), having low to high Si, Al, and Ca, developed in the magnetite-apatite veins in host rocks and in the main ore body, formed during a fluid assisted recrystallization process.

According to the above evidence, it can be inferred that Chadormalu magnetite-apatite ore is a Kiruna-type iron oxide deposit, which formed during a magmatic to brine evolutional process that was associated with an increase in Fe content. Hydrothermal annealing, however, formed the last generation of magnetite.

Acknowledgments This research is an extension to Hassan Heidarian's MSc research conducted at UNB. We also thank Chadormalu mine organization and engineering company of KaniKavan Sharq for their valuable helps doing field investigations. DL is supported by a NSERC Discovery grant. We are particularly grateful for the constructive comments of Dr. Walter Pohl and an anonymous reviewer, as well as the associate editor, Prof. Anton Beran and the chief editor, Prof. Lutz Nasdala which helped to improve the manuscript.

References

Barnes SJ, Roeder PL (2001) The range of spinel compositions in terrestrial mafic and ultramafic rocks. J Petrol 42:2279–2302

Barton MD (2014) Iron oxide(−Cu-Au-REE-P-Ag-U-Co) systems. In: Holland H, Turekian K (eds) Geochemistry of mineral deposits. Treatise on Geochemistry, 2nd ed, vol 13. Elsevier, Maryland Heights, pp. 515–541

Bonyadi Z, Davidson GJ, Mehrabi B, Meffre S, Ghazban F (2011) Significance of apatite REE depletion and monazite inclusions in the brecciated Se-chahun iron oxide-apatite deposit, bafq district, Iran: insights from paragenesis and geochemistry. Chem Geol 281: 253–269

Borg S, Liu W, Pearce M, Cleverley J, MacRae C (2014) Complex mineral zoning patterns caused by Ultra-local equilibrium at reaction interfaces. Geology 42:415–418

Borumandi H (1973) Petrograpische und Lagerst attenkundliche untersuchungen der Esfordi-formation zwischen Mishdovan und Kushk bei Yazd/Zentral Iran. Unpublished PhD Thesis, University of Aachen, Germany

Boucher SM, Hannington MD, Dube B (2010) Primary and secondary ore textures in the West Ansil volcanic-hosted massive-sulphide deposit, Noranda mining camp, Rouyn-Noranda, Quebec. Current Research 2010–10. Geol Surv Can

Ciobanu CL, Cook NJ (2004) Skarn textures and a case study: the ocna de fier-dognecea ore field, Banat, Romania. Ore Geol Rev 24:315–370

Daliran F (1990) The magnetite-apatite deposit of Mishdovan, East Central Iran. An alkali rhyolite hosted, "Kiruna type" occurrence in the Infracambrian Bafq metallotect. PhD Thesis, Heidelberger Geowissenschaftliche Abhandlungen, Germany

Daliran F (2002) Kiruna-type iron oxide-apatite ores and apatitites of the bafq district, Iran, with an emphasis on the REE geochemistry of their apatites: In porter TM (ed) hydrothermal iron oxide copper-gold and related deposits: A global perspective, vol 2. PGC Publishing, Linden Park, pp. 303–320

Daliran F, Stosch HG, Williams PJ, Jamali H, Dorri MB (2010) Early-Cambrian iron oxide-apatite-REE (U) deposits of the Bafq district, east-central Iran. Geol Assoc Canada Short Course Notes 20:147–159

Dare SA, Barnes SJ, Beaudoin G, Méric J, Boutroy E, Potvin-Doucet C (2014) Trace elements in magnetite as petrogenetic indicators. Mineral Deposita 49:785–796

Deo B, Dube RK, Chatterji S (1989) Formation of porous magnetite in the initial stage of solid state reduction of hematite by metallic iron. ISIJ Int 29:345–347

Dupuis C, Beaudoin G (2011) Discriminant diagrams for iron oxide trace element fingerprinting of mineral deposit types. Mineral Deposita 46:319–335

Förster H, Jafarzadeh A (1983) The chadormalu iron ore deposits magnetite filled pipes: geodynamic projection Iran. Final Report, GSI, pp. 501–509

Förster H, Jafarzadeh A (1984) The chadormalu iron ore deposit (bafq district, Central Iran), magnetite filled pipes. Neues Jahrb Geol P-A 168:524–534

Förster H, Jafarzadeh A (1994) The bafq mining district in Central Iran: A highly mineralized infracambrian volcanic field. Econ Geol 89: 1667–1721

Haghipour A (1977) Geological Map of Biabanak–Bafq Area.1:500,000, Geol. Surv. Iran

Hahn G, Pflug HD (1980) Ein neuer medusen-fund aus dem jungprakambrium von zentral-Iran. Senck Leth 60:449–461

Heidarian H (2013) Investigation of genetic relations between mineralization, host rocks and metasomatic alterations in chadormalu iron deposit, Central Iran. Unpublished MSc Thesis, Shahid Beheshti University, Iran (in Persian with English abstract)

Heidarian H, Padyar F, Alirezaei S (2012) Fluid inclusion evidence for a hydrothermal origin for magnetite-apatite ores at Chadormalu iron deposit, Bafq District, Central Iran. ACROFI-IV:32–34

Heidarian H, Alirezaei S, Lentz D (in review) Chadormalu Kiruna-type magnetite-apatite deposit, Bafq district, Iran: Insights from hydrothermal alteration evidence, geochemical, fluid inclusion, and sulfur isotopic data. Ore Geol Rev

Hemley JJ, Hunt JP (1992) Hydrothermal ore-forming processes in the light of studies in rock-buffered systems; II, some general geologic applications. Econ Geol 87:23–43

Hu H, Li J, Lentz D, Ren Z, Zhao X, Deng X, Hall D (2014) Dissolution-reprecipitation process of magnetite from the chengchao iron deposit: insights into ore genesis and implication for in situ chemical analysis of magnetite. Ore Geol Rev 57:393–405

Hu H, Lentz D, Li JW, McCarron T, Zhao XF, Hall D (2015) Reequilibration processes in magnetite from iron skarn deposits. Econ Geol 110:1–8

Huberty JM, Konishi H, Heck PR, Fournelle JH, Valley JW, Xu H (2012) Silician magnetite from the dales gorge member of the Brockman Iron Formation, Hamersley Group, Western Australia. Am Mineral 97:26–37

Jami M (2005) Geology, geochemistry and evolution of the Esfordi Phosphate–Iron Deposit, Bafq Area, Central Iran. Unpublished PhD Thesis, University of New South Wales, Australia

Jami M, Dunlop AC, Cohen DR (2007) Fluid inclusion and stable isotope study of esfordi apatite-magnetite deposit, Central Iran. Econ Geol 102:1111–1125

Jonas L, John T, Putnis A (2013) Influence of temperature and Cl on the hydrothermal replacement of calcite by apatite and the development of porous microstructures. Am Mineral 98:1516–1525

Knipping JL, Bilenker LD, Simon AC, Reich M, Barra F, Deditius AP, Lundstorm C, Bindeman I, Munizaga R (2015) Giant Kiruna-type deposits form by efficient flotation of magmatic magnetite suspensions. Geology 43:591–594

Larson JE (1983) Geology, geochemistry and wall-rock alteration at the magusi and new insco massive sulfide deposits, hebecourt township, Northwestern Quebec. Unpublished MSc Thesis, University of Western Ontario, Canada

Liang HY, Sun W, Su WC, Zartman RE (2009) Porphyry copper–gold mineralization at yulong, China, promoted by decreasing redox potential during magnetite alteration. Econ Geol 104: 587–596

Lohberg BEH, Horndhal AK (1983) Ferride geochemistry of Swedish Precambrian iron ores. Mineral Deposita 48:487–504

Makvandi S, Beaudoin G, McClenaghan BM, Layton-Matthews D (2015) The surface texture and morphology of magnetite from the izok Lake volcanogenic massive sulfide deposit and local glacial sediments, Nunavut, Canada: Application to mineral exploration. J Geochem Explor 150:84–103

Mohseni S, Aftabi A (2015) Structural, textural, geochemical and isotopic signatures of synglaciogenic neoproterozoic banded iron formations (BIFs) at bafq mining district (BMD), Central Iran: the possible ediacaran missing link of BIFs in tethyan metallogeny. Ore Geol Rev 71:215–236

Moore F, Modabberi S (2003) Origin of choghart iron oxide deposit, Bafq District, Central Iran: new isotopic and geochemical evidence. J Sci Islamic Republic of Iran 14:259–269

Mousavi Nasab Z (1994) Geology and genesis of Choghart deposit, Bafq area, Central Iran. Unpublished PhD Thesis, Shiraz University, Iran (in Persian with English abstract)

Mücke A (2003) Magnetite, ilmenite, and ulvite in rocks and ore deposits: petrography, microprobe analyses and genetic implications. Miner Petrol 77:215–234

Mücke A, Cabral AR (2005) Redox and nonredox reactions of magnetite and hematite in rocks. Chem Erde-Geochem 65:271–278

Mücke A, Younessi R (1994) Magnetite–apatite deposits, Kiruna-type, along the sanandaj-sirjan and in the bafq area, Iran, associated with ultramafic and calc alkaline rocks and carbonatites. Miner Petrol 50: 219–244

Müller B, Axelsson MD, Ohlander B (2003) Trace elements in magnetite from Kiruna, Northern Sweden, as determined by LA-ICP-MS. J Geol Soc Sweden 125:1–5

Nadoll P, Mauk JL, Hayes TS, Koenig AE, Box SE (2012) Geochemistry of magnetite from hydrothermal ore deposits and host rocks of the Mesoproterozoic Belt supergroup, United States. Econ Geol 107: 1275–1292

Nadoll P, Angerer T, Mauk JL, French D, Walshe J (2014) The chemistry of hydrothermal magnetite: a review. Ore Geol Rev 61:1–32

Nakamura M, Watson EB (2001) Experimental study of aqueous fluid infiltration into quartzite: implications for the kinetics of fluid redistribution and grain growth driven by interfacial energy reduction. Geofluids 1:73–89

Naslund HR, Henriquez F, Nystrom JO, Vivallo W, Dobbs FM (2002) Magmatic iron ores and associated mineralization: examples from the Chilean High Andes and Coastal Cordillera. In: Porter TM (ed) Hydrothermal iron oxide copper-gold and related deposits, A global perspective, vol 2. PGC Publishing, Adelaide, pp. 207–226

NISCO (National Iranian Steel Corporation) (1980) Report on results of search and evaluation works at magnetic anomalies of the Bafq iron ore region during 1976–1979. Unpublished Internal Report

Nold JL, Davidson P, Dudley MA (2013) The pilot knob magnetite deposit in the Proterozoic St. Francois mountains terrane, Southeast Missouri, USA: a magmatic and hydrothermal replacement iron deposit. Ore Geol Rev 53:446–469

Nyström JO, Henriquez F (1994) Magmatic features of iron ores of the Kiruna type in Chile and Sweden: Ore textures and magnetite geochemistry. Econ Geol 89:820–839

Pollok K, Putnis CV, Putnis A (2011) Mineral replacement reactions in solid solution-aqueous solution systems: volume changes, reactions paths and end-points using the example of model salt systems. Am J Sci 311:211–236

Putnis A (2002) Mineral replacement reactions: from macroscopic observations to microscopic mechanisms. Mineral Mag 66:689–708

Putnis A, John T (2010) Replacement processes in the Earth's crust. Elements 6:159–164

Putnis A, Putnis CV (2007) The mechanism of re-equilibration of solids in the presence of a fluid phase. J Solid State Chem 180:1783–1786

Ramezani J, Tucker RD (2003) The saghand region, Central Iran: U–Pb geochronology, petrogenesis and implications for gondwana tectonics. Am J Sci 303:622–665

Ray GE, Webster ICL (2007) Geology and chemistry of the low Ti magnetite-bearing heff Cu-Au skarn and its associated plutonic rocks, heffley Lake, South-Central British Columbia. Explor Min Geol 16:159–186

Sabet-Mobarhan-Talab A, Alinia F, Asadi F (2014) Hydrothermal overprint of the chador-malu Kiruna-type deposit (Bafq District, Central Iran) and associated REE Mobilization: evidence from mineralogy and geochemistry. I J Econ Envir Sci 5:1–14

Samani B (1993) Saghand formation, a riftogenic unit of upper Precambrian in central Iran. Geosci Sci Q J Geol Surv Iran 2:32–45(in Persian with English abstract)

Seo J, Choi SG, Kim DW, Park JW, Oh CW (2015) A new genetic model for the Triassic Yangyang iron-oxide-apatite deposit, South Korea: Constraints from in situ U-Pb and trace element analyses of accessory minerals. Ore Geol Rev 70:110–135

Sharq KK (2003) Geological report and genesis of chadormalu iron ore deposit. Unpublished Internal, Report(in Persian)

Sharq KK (2005) Petrography of lithological units of the chadormalu area. Unpublished Internal, Report(in Persian)

Sillitoe RH, Burrows DR (2002) New field evidence bearing on the origin of the El Laco magnetite deposit, Northern Chile. Econ Geol 97: 1101–1109

Stöcklin J (1971) Stratigraphic lexicon of Iran. Part 1: Central, North and East Iran. Geol Surv of Iran

Stosch HG, Romer RL, Daliran F, Rhede D (2011) Uranium–lead ages of apatite from iron oxide ores of the Bafq District, East-Central Iran. Mineral Deposita 46:9–21

Torab FM, Lehmann B (2007) Magnetite-apatite deposits of the bafq district, Central Iran: apatite geochemistry and monazite geochronology. Mineral Mag 71:347–363

Whitney JA, Hemley JJ, Simon FO (1985) The concentration of iron in chloride solutions equilibrated with synthetic granitic compositions; the sulfur-free system. Econ Geol 80:444–460

Williams PJ, Barton MD, Johnson DA, Fontboté L, De Haller A, Mark G, Oliver NHS, Marschik R (2005) Iron oxide copper-gold deposits: Geology, space-time distribution, and possible modes of origin. Econ Geol 100th Ann Vol: 371–405

Xia F, Brugger J, Chen G, Ngothai Y, O'Neill B, Putnis A, Pring A (2009) Mechanism and kinetics of pseudomorphic mineral replacement reactions: a case study of the replacement of pentlandite by violarite. Geochim Cosmochim Ac 73:1945–1969